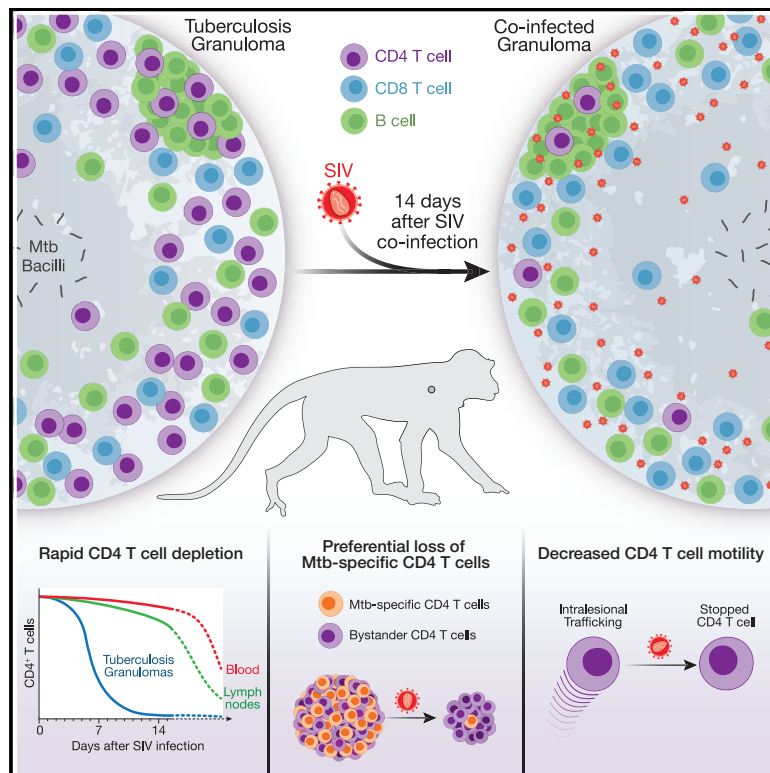**Article**

CD4 T cells are rapidly depleted from tuberculosis granulomas following acute SIV co-infection

Graphical abstract

Authors

Taylor W. Foreman, Christine E. Nelson, Keith D. Kauffman, ..., Juraj Kabat, Laura E. Via, Daniel L. Barber

Correspondence

barberd@niaid.nih.gov

In brief

HIV-mediated destruction of CD4 T cells enhances susceptibility to *Mycobacterium tuberculosis*. Using macaques, Foreman et al. show that CD4 T cells in granulomas are depleted very rapidly after SIV co-infection, indicating that loss of immunity at the site of bacterial replication occurs long before signs of peripheral T cell depletion.

Highlights

- SIV rapidly replicates in Mtb granulomas of co-infected macaques

- Granuloma CD4 T cells are depleted before those in blood, BAL, LNs, or spleen

- CCR5^{+}Eomes[−] Mtb-specific Th1 and Th1[*] cells in granulomas are preferentially depleted

- SIV co-infection reduces motility of CD4 T cells in granulomas

Cell Reports

Article

CD4 T cells are rapidly depleted from tuberculosis granulomas following acute SIV co-infection

Taylor W. Foreman,[1] Christine E. Nelson,[1] Keith D. Kauffman,[1] Nickiana E. Lora,[1] Caian L. Vinhaes,[2,3] Danielle E. Dorosky,[1] Shunsuke Sakai,[1] Felipe Gomez,[4] Joel D. Fleegle,[4] Melanie Parham,[5] Shehan R. Perera,[6] Cecilia S. Lindestam Arlehamn,[7] Alessandro Sette,[7] Tuberculosis Imaging Program,[4] Jason M. Brenchley,[8] Artur T.L. Queiroz,[2,9] Bruno B. Andrade,[2,3] Juraj Kabat,[10] Laura E. Via,[4,11,12] and Daniel L. Barber[1,13,*]

[1]T lymphocyte Biology Section, Laboratory of Parasitic Diseases, National Institute of Allergy and Infectious Disease, National Institutes of Health, Bethesda, MD 20892, USA
[2]Multinational Organization Network Sponsoring Translational and Epidemiological Research (MONSTER) Initiative, Instituto Gonçalo Moniz, Fundação Oswaldo Cruz, Salvador, BA 41810-710, Brazil
[3]Bahiana School of Medicine and Public Health (EBMSP), Salvador, BA 40296, Brazil
[4]Division of Intramural Research, National Institute of Allergy and Infectious Disease, National Institutes of Health, Bethesda, MD 20892, USA
[5]Axle Informatics, National Center for Advancing Translational Sciences, Bethesda, MD 20892, USA
[6]Department of Electrical and Computer Engineering, The Ohio State University, Columbus, OH 43201, USA
[7]Division of Vaccine Discovery, La Jolla Institute for Immunology, La Jolla, CA 92037, USA
[8]Barrier Immunity Section, Laboratory of Viral Diseases, National Institute of Allergy and Infectious Disease, National Institutes of Health, Bethesda, MD 20892, USA
[9]Data and Knowledge Integration Center for Health (CIDACS), Instituto Gonçalo Moniz, Salvador, BA 40296, Brazil
[10]Biological Imaging Section, Research Technologies Branch, National Institute of Allergy and Infectious Disease, National Institutes of Health, Bethesda, MD 20892, USA
[11]Tuberculosis Research Section, Laboratory of Clinical Immunology and Microbiology, National Institute of Allergy and Infectious Disease, National Institutes of Health, Bethesda, MD 20892, USA
[12]Institute of Infectious Disease & Molecular Medicine and Division of Immunology, Department of Pathology, University of Cape Town, Observatory, Cape Town, 7925, South Africa
[13]Lead contact
*Correspondence: barberd@niaid.nih.gov
https://doi.org/10.1016/j.celrep.2022.110896

SUMMARY

HIV/*Mycobacterium tuberculosis* (Mtb) co-infected individuals have an increased risk of tuberculosis prior to loss of peripheral CD4 T cells, raising the possibility that HIV co-infection leads to CD4 T cell depletion in lung tissue before it is evident in blood. Here, we use rhesus macaques to study the early effects of simian immunodeficiency virus (SIV) co-infection on pulmonary granulomas. Two weeks after SIV inoculation of Mtb-infected macaques, Mtb-specific CD4 T cells are dramatically depleted from granulomas, before CD4 T cell loss in blood, airways, and lymph nodes, or increases in bacterial loads or radiographic evidence of disease. Spatially, CD4 T cells are preferentially depleted from the granuloma core and cuff relative to B cell-rich regions. Moreover, live imaging of granuloma explants show that intralesional CD4 T cell motility is reduced after SIV co-infection. Thus, granuloma CD4 T cells may be decimated before many co-infected individuals experience the first symptoms of acute HIV infection.

INTRODUCTION

Human immunodeficiency virus (HIV) infection gradually depletes circulating CD4 T cells, leading to the development of acquired immunodeficiency syndrome (AIDS) and impaired host resistance to microbial infections. CD4 T cells are essential for control of *Mycobacterium tuberculosis* (Mtb) infection, and tuberculosis (TB) is the leading cause of death in persons living with HIV (PLWH) (World Health Organization, 2019). The extent of peripheral CD4 T cell depletion in PLWH correlates with increasing risk of developing active TB (Geldmacher et al., 2012; Glynn et al., 2008; Okoye and Picker, 2013; van der Sande et al., 2004). However, there is also an increased incidence of

active TB in PLWH that have normal-to-high CD4 T cell counts in blood (Esmail et al., 2018; Glynn et al., 2008). The elevated risk of TB in individuals with normal CD4 T cell counts is incompletely understood, but may reflect detrimental impact of antiviral inflammation (e.g., type I interferons [IFNs]) on anti-mycobacterial innate immunity (Mayer-Barber et al., 2014; Sandler et al., 2014; Zhang et al., 2021), impairment of macrophage function (DiNapoli et al., 2016), or preferential depletion of CD4 T cells in tissues compared with circulation (Brenchley et al., 2004; Geldmacher et al., 2010; Picker et al., 2004).

Mtb persists in granulomas, complex structures comprised of multiple immune cell types, which reproducibly position themselves relative to one another (Pagan and Ramakrishnan,

2018). Although variable by many respects, granulomas can be generally described by a few key features, including: an oft-necrotic, macrophage-rich core where mycobacteria are primarily located (Mattila et al., 2013), a lymphocyte-rich cuff circumscribing the macrophage core (Kauffman et al., 2018), and B cell-rich tertiary lymphoid substructures referred to as granuloma-associated lymphoid tissue (GrALT) located within the lymphocyte cuff or found as proximal granuloma satellites (Phuah et al., 2012; Ulrichs et al., 2004). CD4 T cells are primarily found in the lymphocyte cuff but can also be seen interacting with macrophages in the core or with B cells in GrALT (Kauffman et al., 2018). Due to the difficulty of studying human lung infections, little is understood about the effects of HIV infection on Mtb granulomas. Previous studies have shown that simian immunodeficiency virus (SIV) infection of macaques recapitulates the gradual loss of circulating CD4 T cells and eventual development of active tuberculosis disease as seen in humans (Diedrich et al., 2020; Foreman et al., 2016, 2017a, 2017b; Larson et al., 2021; Mehra et al., 2011). Here, we examine the very early effects of SIV infection on CD4 T cell responses at the site of Mtb infection in rhesus macaques to ask if CD4 T cells within the granuloma microenvironment are differentially susceptible to dysfunction and depletion during SIV infection compared with T cells in circulation or lymphoid tissues.

RESULTS

SIV infection of Mtb granulomas

To study the early effects of SIV co-infection in Mtb infection, 10 Indian rhesus macaques were intrabronchially infected with ~56 colony-forming units (CFU) of Mtb H37Rv bilaterally (Figure 1A). Animals were monitored for signs of disease for 10–11 weeks before allocation into groups that either remained Mtb mono-infected (n = 5) or were intravenously infected with 3,000 median tissue culture infectious dose (TCID$_{50}$) of SIVmac239 (n = 5). The study was concluded 14 days after SIV infection and mono-infected controls were time-matched. Animals did not show signs of tuberculosis disease as measured by weight loss or fever over the course of the study (Figures S1A and S1B). Plasma SIV viral loads continuously increased in most animals until day 14 (Figure 1B). Using RNAscope to study SIV localization, viral RNA was detected in granulomas, surrounding lung tissue, and pulmonary lymph nodes (LNs) (Figures 1C and S1H–S1K). Spot density of SIV RNA was higher in granulomas than LNs and surrounding uninvolved lung tissues (Figure 1D). Spots of viral RNA staining in granulomas were further analyzed for their distribution in the core, cuff, or GrALT, as confirmed by CD20-rich areas (Figure S1L). Viral RNA staining was most dense in GrALT regions compared with the core and cuff of the granuloma (Figure 1E). Although it is difficult to distinguish between individual viral particles and infected cells with this technique, we did find that the size of individual spots was different between tissues. LNs contained a higher frequency of large spots >100 μm^2 (possibly representing infected cells) compared with the granulomas (Figure 1F). Overall, these results demonstrate that granulomas become heavily infected with virus quickly after SIV infection.

To determine if SIV co-infection led to changes in TB lesions, macaques were imaged using ^{18}FDG PET-CT scanning before

and 12 days after SIV co-infection or as time-matched controls (Figure 1G). There were no changes in the number of lesions that could be identified by PET-CT imaging after SIV infection (Figure S1C). Among the detectable lesions, we found no difference in granuloma size as measured by volume of abnormal voxels or density range (Figure 1H) or glycolytic activity as measured by ^{18}F-FDG uptake (Figure 1I) between the pre- and post-SIV co-infection time points. While there was no difference in lesions visible by PET/CT imaging, more granulomas were isolated from co-infected macaques at necropsy (Figure S1D). This difference is likely due to the fact that lesions below 2 mm are difficult to observe in scans but are easily found at necropsy. Granulomas in SIV co-infected animals were slightly larger and tended to have increased cellularity, but this did not reach statistical significance (Figures S1E and S1F). Mycobacterial loads in individual granulomas were significantly increased in the co-infected animals, but the difference was less than 2-fold (~625 CFU in SIV-uninfected granulomas versus ~955 CFU in co-infected granulomas) (Figure 1J). Finally, there was no significant correlation between SIV viral and mycobacterial loads in granulomas, indicating that the granulomas with lower viral loads were not different due to their mycobacterial burdens (Figure 1K). Thus, as expected, we did not observe clinically significant tuberculosis disease reactivation in the first 2 weeks after SIV infection; however, it is possible that bacterial loads were just beginning to increase and new granulomas to form.

Soluble mediators in mono- and co-infected granulomas

Next, we examined the effect of acute SIV infection on the pattern of soluble markers of inflammation in granulomas. The markers that correlated with bacterial loads were different in mono- versus co-infected granulomas (Figure 2A). Concentrations of CCL2, CCL4, IL-8, and IL-1RA were positively correlated with mycobacterial burden in the granulomas of both groups of animals. In contrast, IL-6 and IL-1β levels only correlated with CFU in mono-infected granulomas, and CCL3, TNF, CXCL12, and GM-CSF correlated with CFU only in the SIV co-infected granulomas (Figure 2A). SIV loads in granulomas were most strongly correlated with CXCL11 (an IFN-inducible CXCR3 ligand) and to a lesser extent with CCL3 and CCL4 (both CCR5 ligands) as well as TNF, IL-18, and IL-23 (Figure 2A). SIV-infected granulomas contained higher levels of CCL3 and IL-8, but the differences were less than ~2-fold, and the granulomas from SIV-infected and co-infected animals contained very similar levels of the soluble mediators measured here (Figure 2B). Thus, although SIV infection did not dramatically impact the overall levels of soluble mediators in the first 2 weeks after infection, it altered the relationship between mycobacterial loads and inflammatory mediators in granulomas.

To further characterize the impact of early SIV infection on the inflammatory milieu of granulomas, we next used network density analysis of Spearman correlations (Kauffman et al., 2021; Vinhaes et al., 2021) to quantify the interconnectivity of these variables (Figure 2C). After SIV infection, multiple soluble mediators, in particular several chemokines, had increased numbers of correlations with each other, and the overall network density was significantly higher in co-infected granulomas (Figure 2D). Most notably, CXCL12 had no significant correlations with other
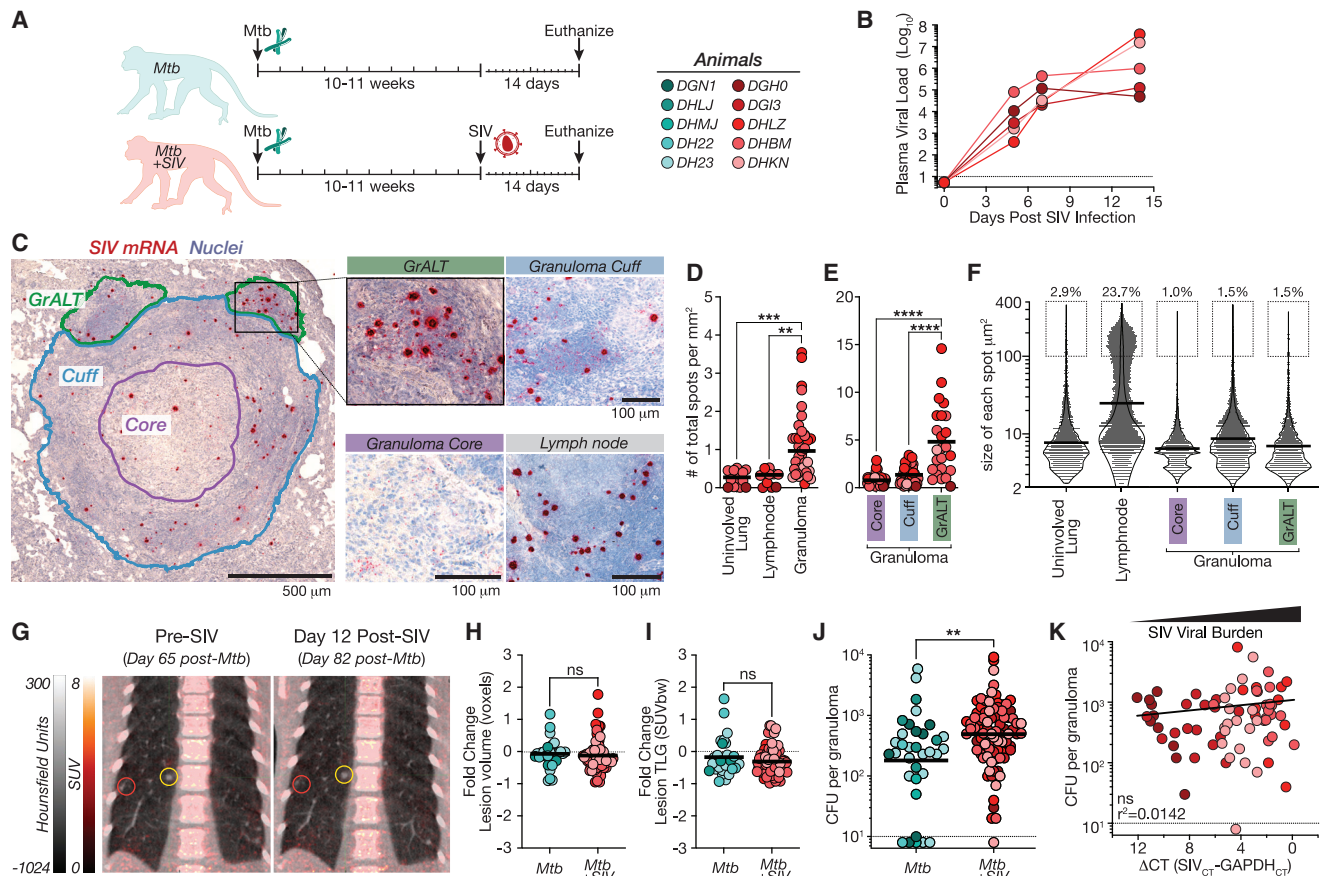
Figure 1. Lung Mtb granulomas are heavily infected by SIV rapidly after co-infection

(A) Ten rhesus macaques were intrabronchially infected with *Mycobacterium tuberculosis* H37Rv for 10–11 weeks and five macaques were subsequently infected with SIVmac239 intravenously. Both groups were followed for another 14 days.

(B) Acute viral infection was tracked by measuring plasma viral loads after co-infection.

(C and D) (C) Example image of RNAscope staining for SIV viral RNA in a co-infected granuloma, including specific microanatomical regions within the granuloma. vRNA, red; counterstained nuclei, light blue. (D) Quantification of the number of SIV$^+$ spots in uninvolved lung tissue (n = 14) and pulmonary lymph nodes (n = 11) compared with granulomas (n = 37).

(E) Microanatomical regions of the granuloma were spatially characterized for different viral burdens. A total of 37 granulomas were analyzed containing 24 GrALT regions.

(F) Distribution violin plots of the size in μm^2 of individual SIV$^+$ spots with the frequency of >100 μm spots indicated above the boxed area in uninvolved lung (n = 5,567), lymph node (n = 28,447), and granuloma core (n = 7,789), cuff (n = 17,639), and GrALT (n = 3,304).

(G) ^{18}FDG PET-CT scans were performed immediately before SIV infection and at day 12 post co-infection, which allowed tracking of 102 visible lesions (n = 5–41 per animal that had detectable lesions).

(H) The change in volume of each lesion as measured in voxels (0.5 mm^3) with abnormal Hounsfeld unit density (−400 to 200 HU) on CT was insignificant from pre- to post-SIV infection.

(I) ^{18}FDG uptake, expressed as the total lesion glycolytic (TLG) activity in standardized uptake value/body weight (SUVbw)/mL, of each lesion was compared pre- to post-SIV infection.

(J) Individual granulomas were isolated at the time of necropsy for determination of bacterial load (n = 2–24 per animal; see Figure S1G).

(K) RNA isolated from each granuloma was assayed for viral quantification and compared with bacterial burden in 72 co-infected granulomas.

Statistical analysis was calculated using (D and E) one-way ANOVA with Tukey correction for multiple comparisons, (H and I) Student's unpaired t tests, (J) Mann-Whitney U test, or (K) nonlinear regression analysis. Ns, non-significant; **p < 0.01, ***p < 0.001 ****p < 0.0001. See also Figure S1.

mediators in the mono-infected granulomas but was the largest node in the co-infected granulomas. Comparing the degrees of connection from the bootstrap analysis highlighted the increased connectivity of CCL3, CCL4, and CXCL12 in co-infected granulomas, while IL-1β showed increased connectivity in mono-infected granulomas (Figure 2E). Such increased network density has previously been shown to reflect heightened

inflammatory states (Bruyn et al., 2021; Tiburcio et al., 2021; Vinhaes et al., 2021). Interestingly, IFN-α was not detected in the granulomas from either group of animals, so we are unable to implicate virus-induced type IFN response in these changes in the granuloma inflammatory milieu after SIV infection (Figure 2F). When taken together with the overall lack of major increases in the total concentrations of most mediators, and the very small
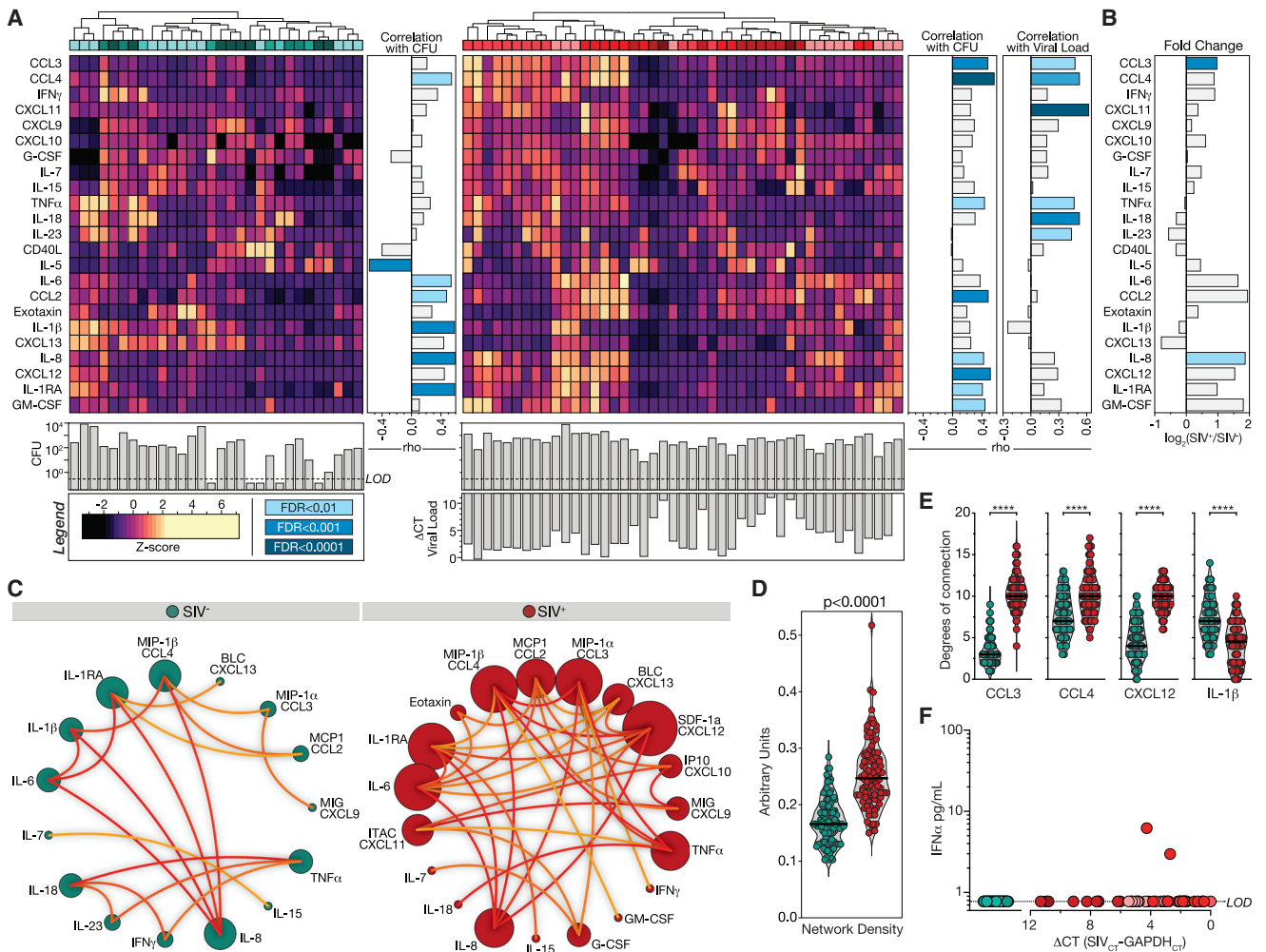
Figure 2. Early changes in soluble mediators in Mtb granulomas after SIV co-infection

(A) Granuloma homogenates were assayed for soluble mediators of inflammation, values normalized to protein levels and by *Z* score and compared with bacterial and viral burdens in 30 granulomas from Mtb mono-infected and 47 granulomas from co-infected macaques. Heatmap visualization of 23 markers within mono-infected (left) and co-infected (right) granulomas with indicated bacterial burden for each granuloma shown below the heatmap, and Spearman correlations with pathogen burdens to the right. Correlations were calculated intra-group and only values with false discovery rate below 0.01 highlighted as significant.

(B) The log2 fold change of soluble markers between mono- and co-infected groups were calculated and compared for significance.

(C) Correlation network analysis using Spearman's rank test were performed and visualized using circus plots, where the size of the circle indicates the number of significant correlations.

(D and E) (D) The overall distribution of network density degree and (E) individual degrees of connectivity of CCL3, CCL4, CXCL12, and IL-1β in 100 bootstrap replicates.

(F) The levels of IFN-α in granuloma homogenates of all samples shown in correlation to viral burden.

Statistical analysis was performed using (A) Spearman's rank test for correlations, (B, D, and E) Student's t test with false discovery ratio correction, or (E) Wilcoxon signed-rank test.

increase in bacterial loads, we speculate these data indicate that, at 14 days after viral infection, SIV may be just beginning to drive increased mycobacterial loads and perturb inflammatory responses.

SIV-mediated depletion of Mtb-specific CD4 T cells in granulomas

We next examined T cell composition after co-infection (Figure S2). The frequency of CD4 T cells was not significantly

different across peripheral blood mononuclear cells (PBMCs), pulmonary LNs, splenocytes, and bronchoalveolar lavage (BAL) (Figure 3A). In contrast, CD4 T cells were greatly reduced in SIV co-infected granulomas on day 14 after SIV infection (Figure 3A). Accordingly, there was no difference in the frequency of CD8 T cells in the BAL, LNs, or spleen, but an increase was observed in granulomas from co-infected animals (Figure S3A). The difference in the CD4:CD8 T cell ratio was different between Mtb mono-infected and Mtb/SIV co-infected
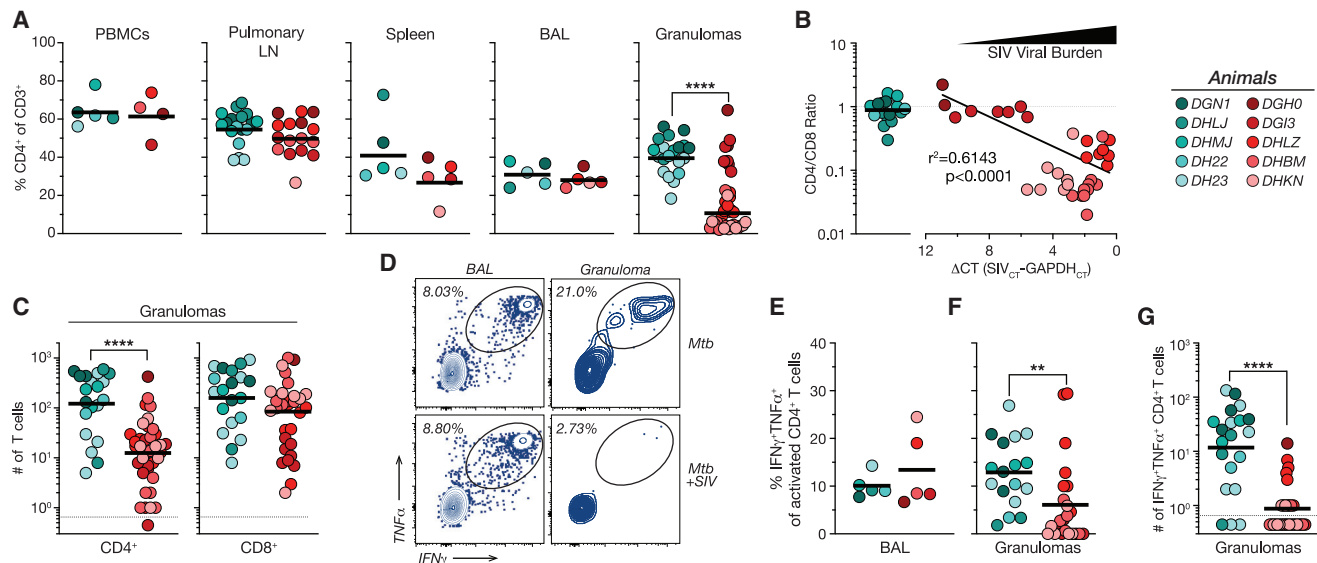
Figure 3. Mtb-specific CD4 T cells are massively depleted in granulomas 2 weeks after SIV co-infection

(A) Flow cytometric analysis of PBMCs, pulmonary lymph nodes (LNs) (n = 1–4/animal), splenocytes, bronchoalveolar lavage (BAL), and individual granulomas with detectable lymphocytes (n = 2–10 per animal; see Figure S1G) showing the percentage of $CD3^+$ T cells that are $CD4^+$.

(B) Comparison of the CD4:CD8 ratio to the viral burden in individual granulomas.

(C) Quantification of the number of total $CD4^+$ and $CD8^+$ T cells in granulomas.

(D) Example flow cytometry plots of Mtb antigen-stimulated $CD4^+$ T cells in BAL and granulomas from mono- and co-infected (top and bottom row, respectively).

(E and F) Frequency of antigen-specific $CD4^+$ T cells in (E) BAL and (F) granulomas after Mtb peptide restimulation.

(G) Absolute number of Mtb-specific $CD4^+$ T cells isolated from individual granulomas.

Statistical analysis was calculated using (A and C–G) Mann-Whitney U test or (B) linear regression analysis. **p < 0.01, ****p < 0.0001. See also Figures S2 and S3.

granulomas (p < 0.0001), and the decline in the CD4:CD8 cell ratio was correlated with SIV viral burden (Figure 3B). Absolute numbers of CD4 T cells were significantly reduced in co-infected compared with mono-infected granulomas, while CD8 T cell numbers were retained (Figure 3C). A total of 60.5% of co-infected granulomas contained less than 20 CD4 T cells and were therefore excluded from further phenotypic analysis. Interestingly, MTB300 peptide-specific CD4 T cells were maintained in the pulmonary LNs and BAL after SIV co-infection (Figures 3E and S3B) but were strikingly reduced in granulomas, where the majority of granulomas no longer contained any Mtb-specific CD4 T cells (Figures 3F and 3G). The Mtb peptide pool used in this study is not optimized for restimulation of CD8 T cells; however, Ag-specific CD8 T cells could still be detected and were not different in any tissue sites of the mono- and co-infected animals (Figures S3C and S3D). Taken together, these results demonstrate that CD4 T cells, particularly Mtb-specific CD4 T cells, are depleted from granulomas prior to detectable depletion in peripheral tissues or even BAL, and that the decline in CD4 T cells is correlated with the viral burden of individual granulomas.

CD4 T cells are variably susceptible to SIV-mediated depletion based on activation and differentiation state and expression viral entry co-receptors (e.g., CCR5) (Geldmacher et al., 2010; Okoye et al., 2007). To examine the differential susceptibility of granuloma CD4 T cell subsets to SIV co-infection, we analyzed T cells for the expression of chemokine receptors CCR5, CCR6, CXCR3, and CXCR5, and the transcription factor Eome-

sodermin (Eomes) (Figures 4A and 4B). We focused on the bulk population of non-naive ($CD95^+$) CD4 T cells, due to the near complete absence of Mtb-specific CD4 T cells in most of the co-infected granulomas. While there was no difference in the frequency of expression of these markers in BAL CD4 T cells (Figure 4C), there was a significant reduction in CCR5- and CXCR3-expressing cells, and no difference in CCR6, CXCR5, or eomes expression in CD4 T cells from co-infected compared with mono-infected granulomas (Figure 4D). We noticed that granulomas from animal DH23 was clustered at the higher end of the distribution of $CCR5^+$, so we tested if the difference between groups remained when this animal was excluded from the analysis. The frequency of $CCR5^+$ cells was still significantly lower in the co-infected animals (p = 0.02). This difference was mirrored in the draining pulmonary LNs where CCR5- and CXCR3-expressing CD4 T cells declined in frequency (Figure S4A). Boolean gating of these markers allowed us to discriminate between several relevant T cell subsets: $CXCR3^+CCR6^-$ Th1 cells, $CCR6^+CXCR3^+$ T_H1^* cells (Acosta-Rodriguez et al., 2007; Arlehamn et al., 2014), $CCR6^+CXCR3^-$ Th17-like, and $CXCR5^+$ Tfh-like cells (Figure 4E). We were able to further subdivide each of these subsets based on expression of the viral entry co-receptor CCR5 as well as eomes. There was no difference between these subsets in the BAL CD4 T cells (Figure 4F). However, among both Th1 and Th1* cells, we found that the $CCR5^+eomes^-$ subsets were preferentially depleted from granulomas (Figure 4G). In contrast, $CCR5^+$ Th1 and Th1* cells expressing eomes did not display evidence of preferential
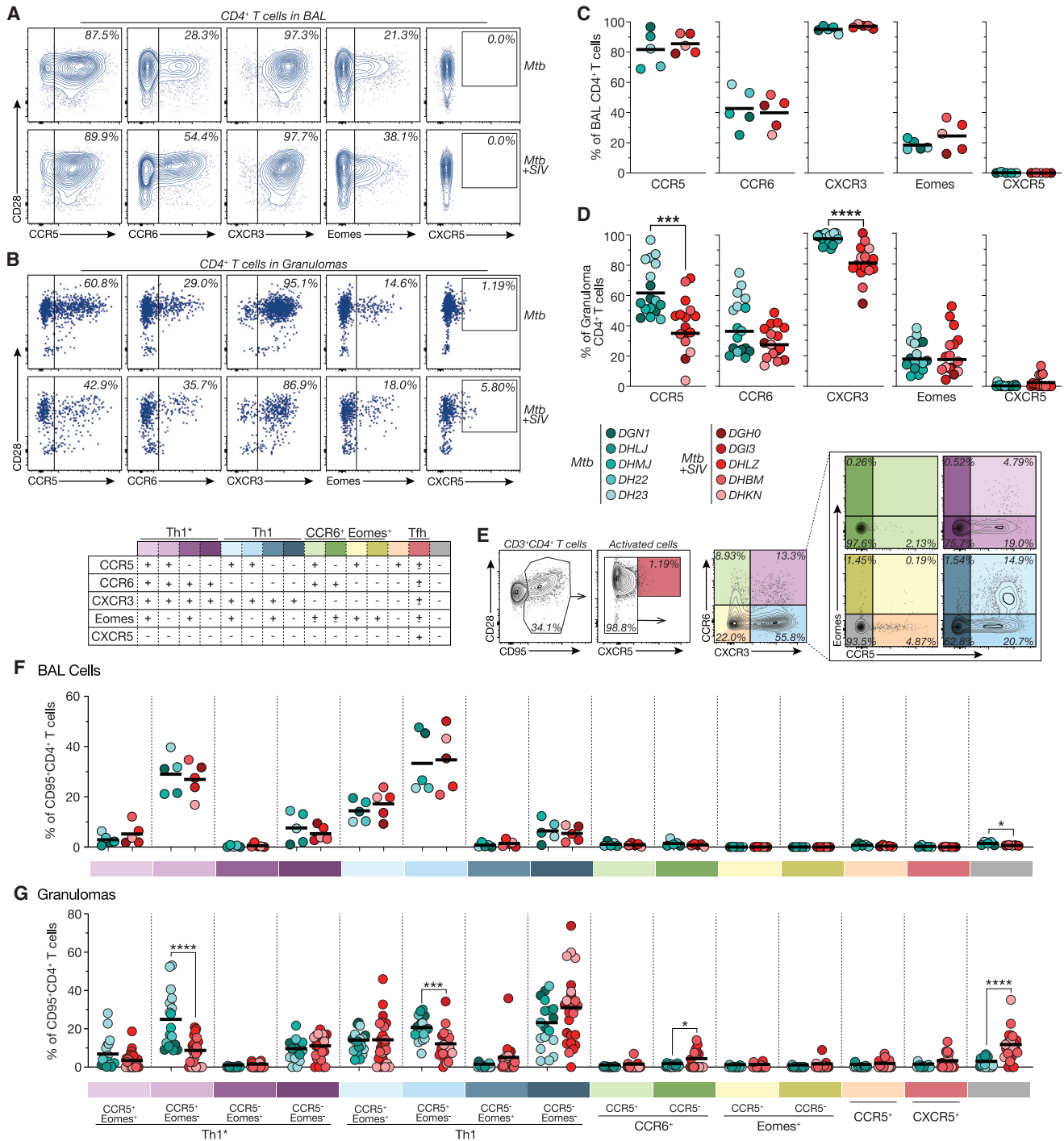
Figure 4. CCR5-expressing Th1 and Th1* cells in granulomas are preferentially depleted by SIV co-infection

(A and B) Example flow cytometry plots of activated CD4 T cells in (A) BAL and (B) granulomas expressing chemokine receptors CCR5, CCR6, CXCR3, and CXCR5, and the transcription factor Eomesodermin (Eomes). Flow cytometry plots of granuloma cells are concatenated files of all granulomas from an individual animal.

(C and D) The frequency of CD4 T cells expressing these markers in the (C) BAL (n = 5) and (D) in individual granulomas (n = 14–17).

(E) Example flow cytometry plots of CD4 T cells from a lymph node demonstrating the Boolean gating analysis.

(F and G) Boolean analysis of the 15 populations of cells in both (F) BAL and (G) individual granulomas.

Statistical analysis was calculated using (C and D) Mann-Whitney U test or (F and G) two-way ANOVA with Šidák correction for multiple comparisons. *p < 0.05, ***p < 0.001, ****p < 0.0001, See also Figure S4.
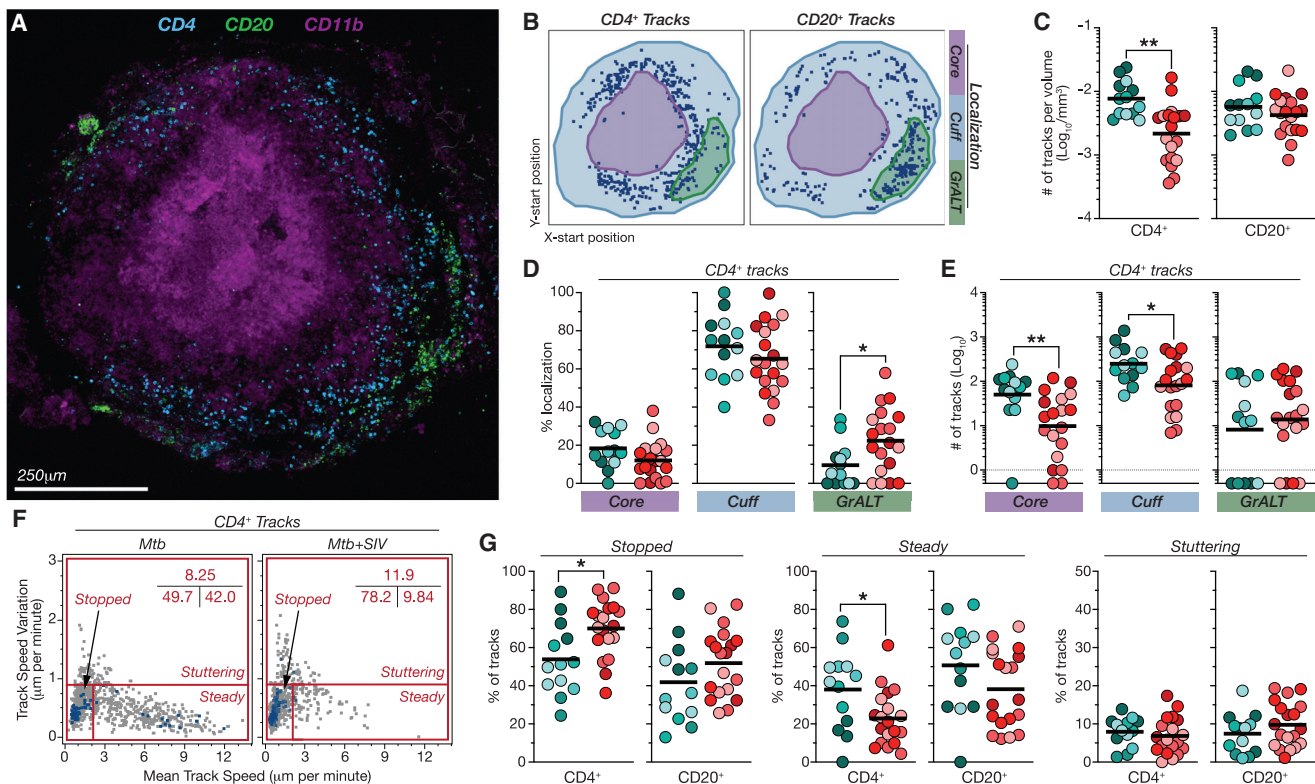
Figure 5. SIV co-infection alters the spatial distribution and intralesional motility of CD4 T cells in Mtb granulomas

(A and B) Example (A) static image of a granuloma used for 4D imaging where (B) distilled cellular tracks from CD4$^+$ and CD20$^+$ cells are shown in the x- and y-start position.

(C) Absolute number of tracks normalized to the volume of tissue imaged (n = 13–19).

(D and E) Localization of CD4$^+$ tracks within the macrophage-rich core, the lymphocyte dense cuff, or the granuloma-associated lymphoid tissue that forms within the cuff as the frequency of or absolute number of total CD4$^+$ tracks in the granuloma.

(F) Example plots of the movement of CD4$^+$ tracks from a mono- and co-infected granuloma, with frequency denoted in the top right corner.

(G) Quantification of the movement of CD4$^+$ tracks and CD20$^+$ tracks as denoted as stopped, steadily moving, or stuttering.

Statistical analysis was calculated using Mann-Whitney U tests. *p < 0.05, **p < 0.01. See also Figure S5.

depletion. As mentioned above, we noted that granulomas from animal DH23 tended to be on the higher end of the distribution of these markers, so we again tested for differences after excluding this animal. All differences remained statistically significant except for CXCR3$^-$CCR6$^+$ cells when the granulomas from DH23 were excluded. CD4 T cells from LNs also displayed a reduction in CCR5$^+$ Th1 cells, while T cells from the spleen and PBMCs did not (Figures S4B–S4E). Thus, while the overall population of CD4 T cells in granulomas is greatly reduced, there is evidence of preferential depletion of Th1 and Th1* CD4 T cells that express CCR5 but lack eomes. Future experiments are needed to explore the role of eomes in determining the susceptibility of CCR5$^+$ CD4 T cells to SIV-mediated depletion.

Intralesional localization and motility of CD4 T cells

To determine the early effects of SIV infection on granuloma architecture and intralesional T cell trafficking, we performed live imaging of granuloma thick-section explants (Kauffman et al., 2021). Live sections of granulomas were stained with antibodies to CD4, CD20, and CD11b and imaged at 37°C for 1–2 h

(Figure 5A; Video S1). Quality control was performed to remove tracks with less than five spots or whose movement was restricted by edges in the x, y, and z planes (Figures S5A and S5B). The x- and y-start positions of the tracks analyzed from the granuloma shown in (Figure 5A) can be seen for CD4$^+$ tracks and CD20$^+$ tracks (Figure 5B). As expected, the number of tracks normalized to the volume of tissue imaged in each granuloma was significantly lower for CD4$^+$ tracks in co-infected compared with mono-infected granulomas, but there was no difference in CD20$^+$ tracks between the groups (Figure 5C). Accordingly, the ratio between CD4$^+$ and CD20$^+$ tracks was statistically significantly reduced in granulomas imaged from co-infected macaques (Figure S5C). We next quantified the localization of tracks within the macrophage-rich core, lymphocyte-rich cuff, or B cell-rich GrALT regions of granulomas (Figure 5B). In SIV co-infected granulomas, the frequency of CD4$^+$ tracks localized to GrALT was increased, likely due to a reduction in the absolute number of tracks found in the core and cuff (Figures 5D and 5E). In contrast, the distribution of CD20$^+$ tracks to different regions of the granuloma was not different between

mono- and co-infected granulomas (Figures S5D and S5E). These results demonstrate CD4 T cells in the core and cuff (i.e., CD4 T cells best positioned to interact with Mtb-infected macrophages) are preferentially depleted early after SIV infection.

We next compared CD4 T cell and B cell movement in mono- and co-infected granulomas. Individual tracks were categorized based on their mean speed and the variation in speed into three major patterns of cellular motility: stopped cells, stuttering cells, or steadily moving cells (Figure 5F). CD4+ tracks displayed reduced motility demonstrated by a significant increase in stopped tracks and concordant decrease in steadily moving tracks (Figure 5G). This difference was not seen in CD20+ tracks, where there was no difference in stopped, steady, or stuttering tracks in mono- versus co-infected granulomas (Figure 5G). This difference was even more significant when pairing the analysis of CD4+ and CD20+ tracks from the same granuloma, indicating the changes in CD4 T cell motility are not due to overall loss of lymphocyte movement in co-infected granulomas (Figure S5F). Taken together these results demonstrate that SIV co-infection significantly decreased CD4 T cell movement in granulomas.

DISCUSSION

CD4 T cell depletion is considered the primary mechanism by which HIV infection leads to the inability to control growth of Mtb, but little is understood about the impact of HIV infection on CD4 T cells at the sites of mycobacterial infection in the tissues. Here, we used a non-human primate (NHP) model of TB and SIV co-infection to study the early events of SIV infection on CD4 T cells in Mtb granulomas. We find that CD4 T cells in granulomas are highly sensitive to SIV-mediated depletion compared with other tissues. It is not clear why granuloma CD4 T cells are so susceptible to SIV-mediated depletion. The selective loss of granuloma CD4 T cells may be due to enhanced permissiveness of these T cells to SIV infection compared with CD4 T cells in other locations (e.g., CCR5-expressing T cells are enriched in granulomas) (Paiardini et al., 2011). It is also possible that the microenvironment of the granuloma itself may facilitate depletion of CD4 T cells. For example, activated macrophages efficiently take up infected CD4 T cells (Calantone et al., 2014), and granulomas are densely packed with macrophages. Importantly, these two possibilities are not mutually exclusive. We cannot rule out the possibility that the loss of CD4 T cells in co-infected granulomas is a result of redistribution to other tissue sites. However, there is precedent for the rapid depletion of CD4 T cells in non-lymphoid tissues, such as the gastrointestinal tract (Brenchley et al., 2008; Mattapallil et al., 2005; Okoye et al., 2007; Veazey et al., 2000).

In some granulomas, there was a near total loss of CD4 T cells within 14 days, indicating that most (perhaps all) T cells in granulomas are susceptible to depletion during SIV co-infection. Nonetheless, our data also indicate that some granuloma CD4 T cells are more susceptible than others. Previous reports have shown that, in persons latently infected with Mtb, HIV co-infection preferentially infects and depletes Mtb-specific CD4 T cells (Amelio et al., 2019; Bunjun et al., 2021; Geldmacher

et al., 2008, 2010; Strickland et al., 2017). Perhaps most importantly, our data show that Mtb-specific CD4 T cells were greatly reduced in frequency in SIV co-infected granulomas long before depletion manifested in blood. CCR5-expressing Th1 and Th1* cells, which have been implicated as a key subset associated with host-protection (Acosta-Rodriguez et al., 2007; Arlehamn et al., 2014), were also reduced in frequency in SIV co-infected granulomas. This is expected as CCR5 is a co-receptor for viral entry. Interestingly, we found that CCR5+ cells that also expressed the transcription factor eomes were not reduced in frequency in co-infected lesions. The mechanisms underlying this apparent differential sensitivity of CCR5+eomes+ CD4 T cells is not clear. Expression of CCR5 ligands in CD4 T cells has been shown previously to be associated decreased viral replication in viremic patients and elite controllers (Casazza et al., 2009; Kinter et al., 1996), and eomes+ CD4 T cells have been shown to produce high levels of CCL3/MIP-1α (Buggert et al., 2018), which may partly explain the increase of soluble CCL3 in granulomas. Therefore, the preservation of CCR5+eomes+ CD4 T cells in granulomas may reflect protection by CCR5-ligand production.

We observed a regionalized depletion where CD4 T cells were lost to a lesser degree in GrALT compared with the core and cuff of the granuloma. This was not due to a lack of viral replication, as the highest amounts of virus in the granuloma, as detected by RNAscope, were in GrALT structures. Germinal centers have been proposed to be an "immunologically privileged" site for viral persistence, perhaps due to the inability of cytotoxic T cells to interact with infected T_FH CD4 T cells, so it is possible that less effective killing by SIV-specific cytotoxic T cells may be responsible for the decreased depletion of GrALT-resident CD4 T cells (Cadena et al., 2021; Mylvaganam et al., 2017).

We also found that the CD4 T cells remaining in SIV co-infected granulomas demonstrated reduced motility, raising the possibility that SIV-mediated suppression of CD4 T cell movement is another mechanism of immunosuppression. HIV infection has been shown to result in reduced motility of CD4 T cells in response to chemokines in vitro (Cecchinato et al., 2017; Perez-Patrigeon et al., 2009). We should also point out, however, that CD4 T cells in granulomas may also stop moving as a result of interaction with peptide-presenting cells (Egen et al., 2011). The reduced movement of CD4 T cells in co-infected granulomas may also reflect the selective loss of a more motile subset of T cells. For example, it is possible that the reduced motility reflects the selective loss of CCR5+ cells, so the importance of this observation to the loss of bacterial control is not clear. Nonetheless, CD4 T cell interaction with infected macrophages is necessary for control of intracellular mycobacterial growth (Grace and Ernst, 2016; Yang et al., 2018), and it is possible that reduced trafficking of the few remaining CD4 T cells in the granulomas further impairs microbial immunity. We do not know if this defect in T cell motility occurs in other tissues, as we have only imaged lung granulomas for this work. Future studies are needed to address the broader possibility that lentiviral infection results in immunosuppression, not only by killing T cells but also by limiting the mobility the ones that remain.

Collectively, these data show how SIV infection is even more detrimental for Mtb-specific immunity than previous

appreciated. We should point out that we do not exclude other mechanisms of viral infection-enhanced susceptibility to Mtb infection. Indeed, cytomegalovirus infection in humans has been associated with enhanced risk of TB (Martinez et al., 2021; Muller et al., 2019) and influenza infection in mice has been shown to enhance Mtb infection (Redford et al., 2014). SIV preferentially kills Mtb-specific CD4 T cells in granulomas, a phenotypic subset of CD4 T cells correlated with immune control, and CD4 T cells in the subregions of granulomas that are best positioned to interact with Mtb-infected macrophages. To make things worse, it impairs the trafficking of the CD4 T cells that remain. Most patients are just beginning to notice signs and symptoms of HIV infection 14 days after primary infection, yet here we demonstrate that CD4 T cells within the granuloma have already been depleted. These data provide a potential explanation of the increased risk of TB reactivation prior to the loss of peripheral CD4 T cells in HIV infection. Understanding the granuloma-specific mechanisms of CD4 T cell susceptibility to SIV-mediated depletion may lead to intervention strategies to preserve anti-tuberculosis immunity in co-infected individuals.

Limitations of the study

Our approach used a well-characterized model of Mtb/SIV co-infection in Indian-origin rhesus macaques. However, we cannot make conclusions about the early depletion of CD4 T cells in granulomas upon co-infection of other NHP species with different susceptibilities to these two pathogens. We only examined the granulomas 14 days post-SIV infection at which time CD4 T cells from granulomas were already extensively depleted, so we cannot make conclusions about the precise kinetics of CD4 T cell loss in granulomas. We also did not compare CD4 T cells in granulomas with those in the gut, a well-characterized site of rapid SIV-mediated CD4 T cell depletion. Finally, we did not measure SIV-specific T cell responses, so we cannot make conclusions about the relative susceptibility of Mtb- and SIV-specific T cells to SIV-mediated depletion. Further experiments are needed to better understand SIV-mediated CD4 T cell depletion during chronic Mtb infection.

CONSORTIA

The members of the NIAID/DIR Tuberculosis Imaging Program are Ayan Abdi, Joel D. Fleegle, Felipe Gomez, Michaela K. Piazza, Katelyn M. Repoli, Becky Y. Sloan, Ashley L. Butler, April M. Walker, Danielle M. Weiner, Michael J. Woodcock, and Alexandra Vatthauer.

STAR★METHODS

Detailed methods are provided in the online version of this paper and include the following:

- KEY RESOURCES TABLE
- RESOURCE AVAILABILITY
  - Lead contact
  - Materials availability
  - Data and code availability
- EXPERIMENTAL MODEL AND SUBJECT DETAILS

- METHOD DETAILS
  - Tissue processing for cells, bacteria, and virus
  - Multiplex cytokine analysis
  - Cell stimulation and flow cytometry
  - Live confocal imaging of granulomas
  - RNAscope and image analysis
- QUANTIFICATION AND STATISTICAL ANALYSIS

AUTHOR CONTRIBUTIONS

Conceptualization, T.W.F. and D.L.B.; methodology, T.W.F., J.M.B., L.E.V., and D.L.B.; software, M.P., S.R.P., and J.K.; formal analysis, T.W.F., C.E.N., C.L.V., F.G., J.D.F., A.T.L.Q., B.B.A., L.E.V., and D.L.B.; investigation, T.W.F., C.E.N., K.D.K., N.E.L., D.E.D., S.S., and TBIP (Tuberculosis Imaging Program); resources, C.S.L.A., A.S., and J.M.B.; writing – original draft, T.W.F. and D.L.B.; writing – review & editing, T.W.F., C.E.N., J.M.B., A.T.L.Q., B.B.A., L.E.V., and D.L.B.; supervision, L.E.V. and D.L.B.; funding acquisition, T.W.F., L.E.V., and D.L.B.

REFERENCES

Acosta-Rodriguez, E.V., Rivino, L., Geginat, J., Jarrossay, D., Gattorno, M., Lanzavecchia, A., Sallusto, F., and Napolitani, G. (2007). Surface phenotype and antigenic specificity of human interleukin 17-producing T helper memory cells. Nat. Immunol. 8, 639–646. https://doi.org/10.1038/ni1467.

Amelio, P., Portevin, D., Hella, J., Reither, K., Kamwela, L., Lweno, O., Tumbo, A., Geoffrey, L., Ohmiti, K., Ding, S., et al. (2019). HIV infection functionally impairs Mycobacterium tuberculosis-specific CD4 and CD8 T-cell responses. J. Virol. 93, 1–18. https://doi.org/10.1128/JVI.01728-18.

Arlehamn, C.L., Seumois, G., Gerasimova, A., Huang, C., Fu, Z., Yue, X., Sette, A., Vijayanand, P., and Peters, B. (2014). Transcriptional profile of tuberculosis antigen-specific T cells reveals novel multifunctional features. J. Immunol. 193, 2931–2940. https://doi.org/10.4049/jimmunol.1401151.

Beites, T., O'Brien, K., Tiwari, D., Engelhart, C.A., Walters, S., Andrews, J., Yang, H.J., Sutphen, M.L., Weiner, D.M., Dayao, E.K., et al. (2019). Plasticity of the Mycobacterium tuberculosis respiratory chain and its impact on tuberculosis drug development. Nat. Commun. *10*, 4970. https://doi.org/10.1038/s41467-019-12956-2.

Brenchley, J.M., Paiardini, M., Knox, K.S., Asher, A.I., Cervasi, B., Asher, T.E., Scheinberg, P., Price, D.A., Hage, C.A., Kholi, L.M., et al. (2008). Differential Th17 CD4 T-cell depletion in pathogenic and nonpathogenic lentiviral infections. Blood *112*, 2826–2835. https://doi.org/10.1182/blood-2008-05-159301.

Brenchley, J.M., Schacker, T.W., Ruff, L.E., Price, D.A., Taylor, J.H., Beilman, G.J., Nguyen, P.L., Khoruts, A., Larson, M., Haase, A.T., and Douek, D.C. (2004). CD4+ T cell depletion during all stages of HIV disease occurs predominantly in the gastrointestinal tract. J. Exp. Med. *200*, 749–759. https://doi.org/10.1084/jem.20040874.

Du Bruyn, E., Fukutani, K.F., Rockwood, N., Schutz, C., Meintjes, G., Arriaga, M.B., Cubillos-Angulo, J.M., Tiburcio, R., Sher, A., Riou, C., et al. (2021). Inflammatory profile of patients with tuberculosis with or without HIV-1 co-infection: a prospective cohort study and immunological network analysis. Lancet Microbe *2*, e375–e385. https://doi.org/10.1016/s2666-5247(21)00037-9.

Buggert, M., Nguyen, S., McLane, L.M., Steblyanko, M., Anikeeva, N., Paquin-Proulx, D., Del Rio Estrada, P.M., Ablanedo-Terrazas, Y., Noyan, K., Reuter, M.A., et al. (2018). Limited immune surveillance in lymphoid tissue by cytolytic CD4+ T cells during health and HIV disease. PLoS Pathog. *14*, e1006973. https://doi.org/10.1371/journal.ppat.1006973.

Bunjun, R., Omondi, F.M.A., Makatsa, M.S., Keeton, R., Wendoh, J.M., Muller, T.L., Prentice, C.S.L., Wilkinson, R.J., Riou, C., and Burgers, W.A. (2021). Th22 cells are a major contributor to the mycobacterial CD4(+) T cell response and are depleted during HIV infection. J. Immunol. *207*, 1239–1249. https://doi.org/10.4049/jimmunol.1900984.

Cadena, A.M., Ventura, J.D., Abbink, P., Borducchi, E.N., Tuyishime, H., Mercado, N.B., Walker-Sperling, V., Siamatu, M., Liu, P.T., Chandrashekar, A., et al. (2021). Persistence of viral RNA in lymph nodes in ART-suppressed SIV/SHIV-infected Rhesus Macaques. Nat. Commun. *12*, 1474. https://doi.org/10.1038/s41467-021-21724-0.

Calantone, N., Wu, F., Klase, Z., Deleage, C., Perkins, M., Matsuda, K., Thompson, E.A., Ortiz, A.M., Vinton, C.L., Ourmanov, I., et al. (2014). Tissue myeloid cells in SIV-infected primates acquire viral DNA through phagocytosis of infected T cells. Immunity *41*, 493–502. https://doi.org/10.1016/j.immuni.2014.08.014.

Casazza, J.P., Brenchley, J.M., Hill, B.J., Ayana, R., Ambrozak, D., Roederer, M., Douek, D.C., Betts, M.R., and Koup, R.A. (2009). Autocrine production of β-chemokines protects CMV-specific CD4+ T cells from HIV infection. PLoS Pathog. *5*, e1000646. https://doi.org/10.1371/journal.ppat.1000646.

Cecchinato, V., Bernasconi, E., Speck, R.F., Proietti, M., Sauermann, U., D'Agostino, G., Danelon, G., Rezzonico Jost, T., Grassi, F., Raeli, L., et al. (2017). Impairment of CCR6+ and CXCR3+ Th cell migration in HIV-1 infection is rescued by modulating actin polymerization. J. Immunol. *198*, 184–195. https://doi.org/10.4049/jimmunol.1600568.

Nichole Cline, A., Bess, J.W., Piatak, M.J., and Lifson, J.D. (2005). Highly sensitive SIV plasma viral load assay: practical considerations, realistic performance expectations, and application to reverse engineering of vaccines for AIDS. J. Med. Primatol. *34*, 303–312. https://doi.org/10.1111/j.1600-0684.2005.00128.x.

Diedrich, C.R., Rutledge, T., Maiello, P., Baranowski, T.M., White, A.G., Borish, H.J., Karell, P., Hopkins, F., Brown, J., Fortune, S.M., et al. (2020). SIV and Mycobacterium tuberculosis synergy within the granuloma accelerates the reactivation pattern of latent tuberculosis. PLoS Pathog. *16*, e1008413. https://doi.org/10.1371/journal.ppat.1008413.

DiNapoli, S.R., Hirsch, V.M., and Brenchley, J.M. (2016). Macrophages in progressive human immunodeficiency virus/simian immunodeficiency virus infections. J. Virol. *90*, 7596–7606. https://doi.org/10.1128/JVI.00672-16.

Egen, J.G., Rothfuchs, A.G., Feng, C.G., Horwitz, M.A., Sher, A., and Germain, R.N. (2011). Intravital imaging reveals limited antigen presentation and T cell effector function in mycobacterial granulomas. Immunity *34*, 807–819. https://doi.org/10.1016/j.immuni.2011.03.022.

Esmail, H., Riou, C., du Bruyn, E., Lai, R.P.J., Harley, Y.X.R., Meintjes, G., Wilkinson, K.A., and Wilkinson, R.J. (2018). The immune response to Mycobacterium tuberculosis in HIV-1-Coinfected persons. Annu. Rev. Immunol. *36*, 603–638. https://doi.org/10.1146/annurev-immunol-042617-053420.

Foreman, T.W., Mehra, S., LoBato, D.N., Malek, A., Alvarez, X., Golden, N.A., Bucsan, A.N., Didier, P.J., Doyle-Meyers, L.A., Russell-Lodrigue, K.E., et al. (2016). CD4+ T-cell-independent mechanisms suppress reactivation of latent tuberculosis in a macaque model of HIV coinfection. Proc. Natl. Acad. Sci. U S A *113*, E5636–E5644. https://doi.org/10.1073/pnas.1611987113.

Foreman, T.W., Mehra, S., Lackner, A.A., and Kaushal, D. (2017a). Translational Research in the nonhuman primate model of tuberculosis. ILAR J. *58*, 151–159. https://doi.org/10.1093/ilar/ilx015.

Foreman, T.W., Veatch, A.V., LoBato, D.N., Didier, P.J., Doyle-Meyers, L.A., Russell-Lodrigue, K.E., Lackner, A.A., Kousoulas, K.G., Khader, S.A., Kaushal, D., and Mehra, S. (2017b). Nonpathologic infection of macaques by an attenuated mycobacterial vaccine is not reactivated in the setting of HIV Co-infection. Am. J. Pathol. *187*, 2811–2820. https://doi.org/10.1016/j.ajpath.2017.08.014.

Geldmacher, C., Ngwenyama, N., Schuetz, A., Petrovas, C., Reither, K., Heeregrave, E.J., Casazza, J.P., Ambrozak, D.R., Louder, M., Ampofo, W., et al. (2010). Preferential infection and depletion of Mycobacterium tuberculosis-specific CD4 T cells after HIV-1 infection. J. Exp. Med. *207*, 2869–2881. https://doi.org/10.1084/jem.20100090.

Geldmacher, C., Schuetz, A., Ngwenyama, N., Casazza, J.P., Sanga, E., Saathoff, E., Boehme, C., Geis, S., Maboko, L., Singh, M., et al. (2008). Early depletion of Mycobacterium tuberculosis-specific T helper 1 cell responses after HIV-1 infection. J. Infect. Dis. *198*, 1590–1598. https://doi.org/10.1086/593017.

Geldmacher, C., Zumla, A., and Hoelscher, M. (2012). Interaction between HIV and Mycobacterium tuberculosis: HIV-1-induced CD4 T-cell depletion and the development of active tuberculosis. Curr. Opin. HIV AIDS *7*, 268–275. https://doi.org/10.1097/COH.0b013e3283524e32.

Glynn, J.R., Murray, J., Bester, A., Nelson, G., Shearer, S., and Sonnenberg, P. (2008). Effects of duration of HIV infection and secondary tuberculosis transmission on tuberculosis incidence in the South African gold mines. AIDS *22*, 1859–1867. https://doi.org/10.1097/QAD.0b013e3283097cfa.

Grace, P.S., and Ernst, J.D. (2016). Suboptimal antigen presentation contributes to virulence of Mycobacterium tuberculosis in vivo. J. Immunol. *196*, 357–364. https://doi.org/10.4049/jimmunol.1501494.

Kauffman, K.D., Sakai, S., Lora, N.E., Namasivayam, S., Baker, P.J., Kamenyeva, O., Foreman, T.W., Nelson, C.E., Oliveira-de-Souza, D., Vinhaes, C.L., et al. (2021). PD-1 blockade exacerbates Mycobacterium tuberculosis infection in rhesus macaques. Sci. Immunol. *6*, eabf3861. https://doi.org/10.1126/sciimmunol.abf3861.

Kauffman, K.D., Sallin, M.A., Sakai, S., Kamenyeva, O., Kabat, J., Weiner, D., Sutphin, M., Schimel, D., Via, L., Barry, C.E., 3rd., et al. (2018). Defective positioning in granulomas but not lung-homing limits CD4 T-cell interactions with Mycobacterium tuberculosis-infected macrophages in rhesus macaques. Mucosal Immunol. *11*, 462–473. https://doi.org/10.1038/mi.2017.60.

Kinter, A.L., Ostrowski, M., Goletti, D., Oliva, A., Weissman, D., Gantt, K., Hardy, E., Jackson, R., Ehler, L., and Fauci, A.S. (1996). HIV replication in CD4+ T cells of HIV-infected individuals is regulated by a balance between the viral suppressive effects of endogenous beta-chemokines and the viral inductive effects of other endogenous cytokines. Proc. Natl. Acad. Sci. U S A *93*, 14076–14081. https://doi.org/10.1073/pnas.93.24.14076.

Larson, E.C., Ellis-Connell, A., Rodgers, M.A., Balgeman, A.J., Moriarty, R.V., Ameel, C.L., Baranowski, T.M., Tomko, J.A., Causgrove, C.M., Maiello, P., et al. (2021). Pre-existing simian immunodeficiency virus infection increases expression of T cell markers associated with activation during early Mycobacterium tuberculosis coinfection and impairs TNF responses in granulomas. J. Immunol. *207*, 175–188. https://doi.org/10.4049/jimmunol.2100073.

Martinez, L., Nicol, M.P., Wedderburn, C.J., Stadler, A., Botha, M., Workman, L., le Roux, D.M., and Zar, H.J. (2021). Cytomegalovirus acquisition in infancy and the risk of tuberculosis disease in childhood: a longitudinal birth cohort study in Cape Town, South Africa. Lancet Glob. Health 9, e1740–e1749. https://doi.org/10.1016/S2214-109X(21)00407-1.

Mattapallil, J.J., Douek, D.C., Hill, B., Nishimura, Y., Martin, M., and Roederer, M. (2005). Massive infection and loss of memory CD4+ T cells in multiple tissues during acute SIV infection. Nature 434, 1093–1097. https://doi.org/10.1038/nature03501.

Mattila, J.T., Ojo, O.O., Kepka-Lenhart, D., Marino, S., Kim, J.H., Eum, S.Y., Via, L.E., Barry, C.E., 3rd, Klein, E., Kirschner, D.E., et al. (2013). Microenvironments in tuberculous granulomas are delineated by distinct populations of macrophage subsets and expression of nitric oxide synthase and arginase isoforms. J. Immunol. 191, 773–784. https://doi.org/10.4049/jimmunol.1300113.

Mayer-Barber, K.D., Andrade, B.B., Oland, S.D., Amaral, E.P., Barber, D.L., Gonzales, J., Derrick, S.C., Shi, R., Kumar, N.P., Wei, W., et al. (2014). Host-directed therapy of tuberculosis based on interleukin-1 and type I interferon crosstalk. Nature 511, 99–103. https://doi.org/10.1038/nature13489.

Mehra, S., Golden, N.A., Dutta, N.K., Midkiff, C.C., Alvarez, X., Doyle, L.A., Asher, M., Russell-Lodrigue, K., Monjure, C., Roy, C.J., et al. (2011). Reactivation of latent tuberculosis in rhesus macaques by coinfection with simian immunodeficiency virus. J. Med. Primatol 40, 233–243. https://doi.org/10.1111/j.1600-0684.2011.00485.x.

Muller, J., Tanner, R., Matsumiya, M., Snowden, M.A., Landry, B., Satti, I., Harris, S.A., O'Shea, M.K., Stockdale, L., Marsay, L., et al. (2019). Cytomegalovirus infection is a risk factor for tuberculosis disease in infants. JCI Insight 4, e130090. https://doi.org/10.1172/jci.insight.130090.

Mylvaganam, G.H., Rios, D., Abdelaal, H.M., Iyer, S., Tharp, G., Mavigner, M., Hicks, S., Chahroudi, A., Ahmed, R., Bosinger, S.E., et al. (2017). Dynamics of SIV-specific CXCR5+ CD8 T cells during chronic SIV infection. Proc. Natl. Acad. Sci. U S A 114, 1976–1981. https://doi.org/10.1073/pnas.1621418114.

Okoye, A., Meier-Schellersheim, M., Brenchley, J.M., Hagen, S.I., Walker, J.M., Rohankhedkar, M., Lum, R., Edgar, J.B., Planer, S.L., Legasse, A., et al. (2007). Progressive CD4+ central memory T cell decline results in CD4+ effector memory insufficiency and overt disease in chronic SIV infection. J. Exp. Med. 204, 2171–2185. https://doi.org/10.1084/jem.20070567.

Okoye, A.A., and Picker, L.J. (2013). CD4(+) T-cell depletion in HIV infection: mechanisms of immunological failure. Immunol. Rev. 254, 54–64. https://doi.org/10.1111/imr.12066.

Pagan, A.J., and Ramakrishnan, L. (2018). The formation and function of granulomas. Annu. Rev. Immunol. 36, 639–665. https://doi.org/10.1146/annurev-immunol-032712-100022.

Paiardini, M., Cervasi, B., Reyes-Aviles, E., Micci, L., Ortiz, A.M., Chahroudi, A., Vinton, C., Gordon, S.N., Bosinger, S.E., Francella, N., et al. (2011). Low levels of SIV infection in sooty mangabey central memory CD(4)(+) T cells are associated with limited CCR5 expression. Nat. Med. 17, 830–836. https://doi.org/10.1038/nm.2395.

Perez-Patrigeon, S., Vingert, B., Lambotte, O., Viard, J.P., Delfraissy, J.F., Theze, J., and Chakrabarti, L.A. (2009). HIV infection impairs CCR7-dependent T-cell chemotaxis independent of CCR7 expression. AIDS 23, 1197–1207. https://doi.org/10.1097/QAD.0b013e32832c4b0a.

Phuah, J.Y., Mattila, J.T., Lin, P.L., and Flynn, J.L. (2012). Activated B cells in the granulomas of nonhuman primates infected with Mycobacterium tuberculosis. Am. J. Pathol. 181, 508–514. https://doi.org/10.1016/j.ajpath.2012.05.009.

Picker, L.J., Hagen, S.I., Lum, R., Reed-Inderbitzin, E.F., Daly, L.M., Sylwester, A.W., Walker, J.M., Siess, D.C., Piatak, M., Jr., Wang, C., et al. (2004). Insufficient production and tissue delivery of CD4+ memory T cells in rapidly progressive simian immunodeficiency virus infection. J. Exp. Med. 200, 1299–1314. https://doi.org/10.1084/jem.20041049.

Redford, P.S., Mayer-Barber, K.D., McNab, F.W., Stavropoulos, E., Wack, A., Sher, A., and O'Garra, A. (2014). Influenza A virus impairs control of Mycobacterium tuberculosis coinfection through a type I interferon receptor-dependent pathway. J. Infect. Dis. 209, 270–274. https://doi.org/10.1093/infdis/jit424.

Sandler, N.G., Bosinger, S.E., Estes, J.D., Zhu, R.T.R., Tharp, G.K., Boritz, E., Levin, D., Wijeyesinghe, S., Makamdop, K.N., del Prete, G.Q., et al. (2014). Type I interferon responses in rhesus macaques prevent SIV infection and slow disease progression. Nature 511, 601–605. https://doi.org/10.1038/nature13554.

Strickland, N., Muller, T.L., Berkowitz, N., Goliath, R., Carrington, M.N., Wilkinson, R.J., Burgers, W.A., and Riou, C. (2017). Characterization of Mycobacterium tuberculosis-specific cells using MHC Class II tetramers reveals phenotypic differences related to HIV infection and tuberculosis disease. J. Immunol. 199, 2440–2450. https://doi.org/10.4049/jimmunol.1700849.

Tiburcio, R., Barreto-Duarte, B., Naredren, G., Queiroz, A.T.L., Anbalagan, S., Nayak, K., Ravichandran, N., Subramani, R., Antonelli, L.R.V., Satagopan, K., et al. (2021). Dynamics of T-lymphocyte activation related to paradoxical tuberculosis-associated immune reconstitution inflammatory syndrome in persons with advanced HIV. Front. Immunol. 12, 757843. https://doi.org/10.3389/fimmu.2021.757843.

Ulrichs, T., Kosmiadi, G.A., Trusov, V., Jorg, S., Pradl, L., Titukhina, M., Mishenko, V., Gushina, N., and Kaufmann, S.H. (2004). Human tuberculous granulomas induce peripheral lymphoid follicle-like structures to orchestrate local host defence in the lung. J. Pathol. 204, 217–228. https://doi.org/10.1002/path.1628.

van der Sande, M.A., Schim van der Loeff, M.F., Bennett, R.C., Dowling, M., Aveika, A.A., Togun, T.O., Sabally, S., Jeffries, D., Adegbola, R.A., Sarge-Njie, R., et al. (2004). Incidence of tuberculosis and survival after its diagnosis in patients infected with HIV-1 and HIV-2. AIDS 18, 1933–1941. https://doi.org/10.1097/00002030-200409240-00009.

Veazey, R.S., Tham, I.C., Mansfield, K.G., DeMaria, M., Forand, A.E., Shvetz, D.E., Chalifoux, L.V., Sehgal, P.K., and Lackner, A.A. (2000). Identifying the target cell in primary simian immunodeficiency virus (SIV) infection: highly activated memory CD4(+) T cells are rapidly eliminated in early SIV infection in vivo. J. Virol. 74, 57–64. https://doi.org/10.1128/jvi.74.1.57-64.2000.

Vinhaes, C.L., Carmo, T.A., Queiroz, A.T.L., Fukutani, K.F., Araujo-Pereira, M., Arriaga, M.B., Lacerda, M.V.G., Barral-Netto, M., and Andrade, B.B. (2021). Dissecting disease tolerance in Plasmodium vivax malaria using the systemic degree of inflammatory perturbation. PLoS Negl. Trop. Dis. 15, e0009886. https://doi.org/10.1371/journal.pntd.0009886.

World Health Organization (2019). Global Tuberculosis Report 2019 (World Health Organization). License: CC BY-NC-SA 3.0 IGO. https://apps.who.int/iris/handle/10665/329368.

Yang, J.D., Mott, D., Sutiwisesak, R., Lu, Y.J., Raso, F., Stowell, B., Babunovic, G.H., Lee, J., Carpenter, S.M., Way, S.S., et al. (2018). Mycobacterium tuberculosis-specific CD4+ and CD8+ T cells differ in their capacity to recognize infected macrophages. PLoS Pathog. 14, e1007060. https://doi.org/10.1371/journal.ppat.1007060.

Zhang, L., Jiang, X., Pfau, D., Ling, Y., and Nathan, C.F. (2021). Type I interferon signaling mediates Mycobacterium tuberculosis-induced macrophage death. J. Exp. Med. 218, e20200887. https://doi.org/10.1084/jem.20200887.

STAR★METHODS

KEY RESOURCES TABLE

REAGENT or RESOURCE	SOURCE	IDENTIFIER
Antibodies		
Anti-CD11b (Clone ICRF44) PE	Biolegend	Cat# 301305, AB_314157
Anti-CD183/CXCR3 (Clone G025H7) PE-Cyanine 7	Biolegend	Cat# 353719, AB_11218804
Anti-CD185/CXCR5 (MU5UBEE) FITC	Invitrogen	Cat# 11-9185-42, AB_2572526
Anti-CD195/CCR5 (Clone 3A9) Brilliant Violet 421	BD Biosciences	Cat# 565000, AB_2739038
Anti-CD196/CCR6 (Clone 11A9) Brilliant Ultraviolet 496	BD Biosciences	Cat# 612948 AB_2833076
Anti-CD20 (Clone 2H7) Alexa Fluor 488	Biolegend	Cat# 302316, AB_493227
Anti-CD28 (Clone CD28.2) Brilliant Ultraviolet 737	BD Biosciences	Cat# 612815, AB_2738808
Anti-CD3 (Clone SP34-2) Brilliant Violet 786	BD Biosciences	Cat# 563918, AB_2738487
Anti-CD4 (Clone SK3) Biotin	Biolegend	Cat# 344610, AB_2028490
Anti-CD4 (Clone OKT4) Brilliant Violet 421	Biolegend	Cat# 317433, AB_11150413
Anti-CD8a (Clone RPA-T8) Brilliant Violet 510	Biolegend	Cat# 301047, AB_2561378
Anti-CD95/Fas (Clone DX2) Brilliant Violet 711	Biolegend	Cat# 305643, AB_2629740
Anti-EOMES (clone WD1928) eFluor 660	Invitrogen	Cat# 50-4877-42, AB_2574229
Anti-IFN-γ (Clone B27) Brilliant Violet 605	Biolegend	Cat# 506541. AB_2801101
Anti-TNF (Clone MAb11) Brilliant Ultraviolet 395	BD Biosciences	Cat# 563996, AB_2738533
Human BD Fc Block	BD Biosciences	Cat# 564219, AB_2728082
Streptavidin Brilliant Ultraviolet 805	BD Biosciences	Cat# 564923
Bacterial and virus strains		
Mycobacterium tuberculosis: H37Rv-mCardinal	This paper	N/A
Simian Immunodeficiency Virus: Substrain mac239	This paper	N/A
Chemicals, peptides, and recombinant proteins		
MTB300 epitope peptide pool	Arlehamn et al., 2014	N/A
Ficoll-Paque PLUS	Fisher Scientific	Cat# 45-001-749
Critical commercial assays		
Cytokine & Chemokine 30-plex NHP ProcartaPlex Panel	Invitrogen	Cat# EPX300-40044-901
Quant-iT Protein Assay Kit	Invitrogen	Cat# Q33210
ImmPRESS HRP Horse Anti-mouse IgG PLUS Polymer Kit	Vector Labs	Cat# MP-7802
RNAscope 2.5 HD Assay - RED	ACD Bio	Cat# 322350
TaqPath 1-Step RT-qPCR Kit	ThermoFisher	Cat# A15299
Qiagen RNeasy Plus Kit	Qiagen	Cat# 74106
Experimental models: Organisms/strains		
Macaque monkeys (macaca mulatta)	NIAID breeding colony	N/A
Oligonucleotides		
RNAscope Probe-SIVmac239	ACD Bio	Cat# 312811
GAPDH Assay ID: Rh02621745-g1	ThermoFisher	Cat# 4331182
SIV RT-PCR probe: [FAM] CTTCNTCAGTKTGTTTCACTTTCTCTTCTGCG	Cline, et al., 2005	N/A

Continued

REAGENT or RESOURCE	SOURCE	IDENTIFIER
SIVmac239 primer forward: GTCTGCGTCATNTGGTGCATTC	Cline, et al., 2005	N/A
SIVmac239 primer reverse: CACTAGKTGTCTCTGCACTATNTGTTTTG	Cline, et al., 2005	N/A
Software and algorithms		
R-Bioconductor package Complex Heatmap	https://www.bioconductor.org/packages/release/bioc/html/ComplexHeatmap.html	N/A
CRAN R package Hmisc	https://cran.r-project.org/web/packages/Hmisc/index.html	N/A
CRAN R package viridis	https://cran.r-project.org/web/packages/viridis/vignettes/intro-to-viridis.html	N/A
ggplot2	https://ggplot2.tidyverse.org	N/A
Igraph	https://igraph.org/r/	N/A
FlowJo, v10.8.1	FlowJo, LLC	N/A
QuPath v0.2.3	https://qupath.github.io	N/A
Graphpad Prism v9.3.1	GraphPad	N/A
Imaris v9.7.2	Oxford Instruments	N/A

RESOURCE AVAILABILITY

Lead contact

Further information and requests for resources and reagents should be directed to and will be fulfilled by the Lead Contact: Daniel L. Barber (barberd@niaid.nih.gov).

Materials availability

This work did not generate any unique reagents.

Data and code availability

This paper does not report original code. All software utilized is freely or commercially available and is listed in the Key resources table. All data reported in this paper will be shared by the Lead contact upon request.

EXPERIMENTAL MODEL AND SUBJECT DETAILS

Rhesus macaques originally from the Morgan Island NIH breeding colony were housed in biocontainment according to the Animal Welfare Act and the Guide for the Care and Use of Laboratory Animals within a AAALAC international-accredited animal biosafety level-3 vivarium. Daily enrichment was provided for the macaques. All procedures were performed using anesthetics according to the approved NIAID DIR Animal Care and Use Committee study proposal LPD-25E. Ten male rhesus macaques aged 1.8–3.1 years old were intrabronchially infected with ~56 CFU of *Mycobacterium tuberculosis* (*Mtb*) strain H37Rv-mCardinal (kindly provided by Dr. Clifton Barry III, chief of the Tuberculosis Research Section, Laboratory of Clinical Immunology and Microbiology, NIAID) bilaterally using 2-mL of saline each into the right and left lower lobes (14.0 ± 3.77 CFU/mL). Thereafter animals were randomly assigned to one of two groups where the *mono*-infection group remained SIV-naïve and the co-infection group was intravenously injected with 3,000 $TCID_{50}$ of SIVmac239. Animals were scanned at regular intervals with a LFER 150 PT/CT scanner (Mediso, Inc.) using ^{18}FDG (0.5 mCi/kg) and tubercular lung disease, as well as, individual lesion characteriztics were analyzed on serial scans as described previously (Beites et al., 2019; Kauffman et al., 2021). For tissue collection, a co-infected animal along with a time-matched *Mtb* mono-infected animal was euthanized according to American Veterinary Medical Association guidelines.

METHOD DETAILS

Tissue processing for cells, bacteria, and virus

Blood was collected using EDTA-tubes and cells isolated using Ficoll-Paque Density Centrifugation (GE Life Sciences). Bronchoalveolar lavage (BAL) was collected using a modified feeding tube inserted through the trachea into the lower pulmonary lobes and lavaged using ~60mL of sterile saline. Fluid was then filtered using a 100-micron filter and centrifuged for the collection of cells. Tissues were taken for analysis at the time of necropsy. For single cell suspensions, spleen and lymphnodes were homogenized using

gentleMACSs dissociators (Miltenyi Biotec) and filtered through a 100-micron filter while isolated granulomas were mashed through a 100-micron filter using a syringe plunger. Homogenates from granulomas and tissues were serially diluted and plated on 7H11 agar plates incubated at 37°C for 3–4 weeks before quantification. Granuloma homogenate was taken for RNA isolation using RNeasy Plus Kits and stored at −80°C (Qiagen). Quantification of viral burden was done using TaqPath 1-step RT-qPCR Master Mix (Thermo Fisher Scientific) and primers/probes sets targeting SIVmac239 (Cline et al., 2005) or GAPDH (Thermo Fisher Scientific). Reactions were completed in triplicates for 40 cycles using FAM dyes. Plasma was filter-sterilized and analyzed for plasma viral load by RT-qPCR by Quantitative Molecular Diagnostics Core at the Frederick National Laboratory.

Multiplex cytokine analysis

Granuloma homogenates were filter-sterilized and processed for soluble protein marker concentrations using the Invitrogen Cytokine and Chemokine 30-Plex ProcartaPlex Kit (Thermo Fisher Scientific) according to manufacturer protocol. Samples were acquired using a MAGPIX with xPONENT software (Luminex Corporation). Soluble marker protein levels were normalized to total protein levels measured by Quant-iT protein Assay Kit (Thermo Fisher Scientific).

Cell stimulation and flow cytometry

Cells were stimulated with 2 μg/mL of MTB300 epitope peptide pool (Arlehamn et al., 2014) in the presence of brefeldin A and monensin for 6 h at 37°C in Complete media (RPMI-1640 with 10% fetal calf serum (FCS), 1% Sodium pyruvate, 1% penicillin and strep-tomycin, 25 mM Hepes, and 2 mM l-glutamate). Cells were stained using fixable live/dead stain for 20 min at room temperature. Surface antibody staining was done in PBS containing 1% FCS and 1X Brilliant Stain Buffer (BD Biosciences) for 20 min at room temperature. After fixation and permeabilization using Foxp3/Transcription Factor Staining Kit (eBiosciences), intracellular antibody staining was done in PBS containing 1% FCS, 1X Brilliant Stain Buffer, and 1X Permeabilization reagent for 30 min at 4°C. Samples were acquired using a FACSymphony cytometer (BD Biosciences) and data analyzed using FlowJo 10 (FlowJo, LLC).

Live confocal imaging of granulomas

Isolated granulomas were kept on ice until embedding in PBS with 2% agarose. The tissue was cut into 300-micron thick sections using a Leica VT1000 S Vibrating Blade Microtome (Leica Microsystems) housed in Class II, Biosafety hood within a BSL3 laboratory. Sections of tissue were incubated in 1X PBS supplemented with 10% FCS, isotype-specific blocking antibodies, and Human FC Block (BD Biosciences) for 2–8 h at 4°C. After blocking, tissues were stained with antibodies CD4, CD20, and CD11b for 2–12 h at 4°C with intermittent shaking. Tissues were then washed and placed into chamber slides containing Complete Imaging Media (Complete media made with phenol red-free RPMI) supplemented with ProLong Live Antifade Reagent (Thermo Fisher Scientific). After incubation in a 5% CO$_2$ incubation chamber at 37°C for 1 h, the chambered slide was imaged using Leica SP5 inverted confocal microscope with environmental chamber to maintain the sample humidified at 37°C (Leica Microsystems). Sections were serially imaged over the course of 1–2 h and compiled using LAS X software (Leica Microsystems). Image analysis was performed using Imaris software (Bitplane) for quantification of individual cells using the spot function to track their movement over time. Data from tracks were exported into FlowJo 10 software (FlowJo, LLC) for data visualization and quantification. Briefly, tracks that were limited in movement by the edges of the X-, Y-, or Z-plane were excluded from analysis. Using the X- and Y-starting point of a track, cells could be localized to different areas in the granuloma. Finally, track movement was categorized into three different forms. Stopped and Steady tracks both had ≤0.90 μm/min track speed variation but were characterized by ≤ 2.0 μm/min or >2.0 μm/min mean track speed, respectively. Stuttering tracks had any mean track speed but were characterized by track speed variation >0.90 μm/min.

RNAscope and image analysis

Formalin Fixed Paraffin embedded tissues sections were cut into 10-micron thick sections using RNAse precautions and used for RNAscope *in situ* hybridization staining for viral RNA (ACD Biotechne). Slides were dewaxed using xylene and ethanol and then underwent epitope retrieval using heat induced low-pH methods according to the manufacturer. Slides were then treated with diluted protease plus for 20 min at 40°C and endogenous peroxidases blocked using hydrogen peroxide for 10 min at room temperature. Probes for SIVmac239, containing 83 separate pairs of probes spanning the proviral gag, vif, pol, tat, env, vpx, vpr, nef, and rev genes, were used for single color immunohistochemistry with hematoxylin counter-staining using the RNAscope 2.5 HD Assay-RED (ACD Biotechne). Immunocytochemically stained slides were imaged using Aperio VERSA (Leica Microsystems) and analyzed using quPath to identify spots with pixel size 0.5-microns, background radius 8-microns, median radius 8-microns, sigma 0.75-microns, minimum area 2.0-microns, maximum area 400-microns, with threshold of 0.25. CD20 staining was performed on de-parrafinized slides that underwent epitope retrieval using heat induced low-pH methods. Slides were stained with anti-CD20 for 1 h at room temp. Staining was developed according to ImmPRESS HRP anti-mouse IgG PLUS Polymer Kit (Vector). SIV mRNA spots were then colocalized to granuloma regions using annotation tabs for each area of the granuloma which were identified according to the differential hematoxylin counter-staining patterns and CD20 staining.

QUANTIFICATION AND STATISTICAL ANALYSIS

All statistical analyses were conducted using GraphPad Prism v9 (GraphPad Software), FlowJo v10 (FlowJo, LLC), Imaris (Oxford Instruments), QuPath, R (The R Foundation), or Python (The Python Foundation). Data were tested for Gaussian distribution using the DÁgostino's K-square test. For group comparisons, individual tests vary and are denoted in each figure legend but include two-tailed unpaired T-tests, Mann-Whitney U-test, one-way ANOVA with correction for multiple tests using Tukey Multiple Comparison test corrections, two way ANOVA with Šidák correction for multiple comparisons, non-linear regression analysis of semi-log line, or simple linear regression analysis. Multiplex Luminex assay data were analyzed using R packages *igraph*, *ggplot2*, *viridis*, *ComplexHeatmap*, *Hmisc*, with *p.adjust* function. Fold change was measured and significance test by Student's T test with False Discovery Ratio correction. Correlation analyses were performed using the Spearman's rank test with 100 bootstrap replicates. Bootstrap threshold value was defined in 80 replicates. Significant values were corrected using False Discovery Ratio. Any place p-value are reported in asterisks * $p < 0.05$, ** $p < 0.01$, *** $p < 0.001$, and **** $p < 0.0001$, ns = non-signficant.